

Coulomb interactions and effective quantum inertia of charge carriers in a macroscopic conductor

A. Delgard¹, B. Chenaud¹, U. Gennser², A. Cavanna², D. Mailly², P. Degiovanni³ and C. Chaubet¹

¹ *Université Montpellier 2, Laboratoire Charles Coulomb UMR5221, F-34095, Montpellier, France
CNRS, Laboratoire Charles Coulomb UMR5221, F-34095, Montpellier, France*

² *Centre de Nanosciences et de Nanotechnologies (C2N), CNRS,
Université Paris-Sud, Université Paris-Saclay, 91120 Palaiseau, France and*

³ *Univ Lyon, Ens de Lyon, Université Claude Bernard Lyon 1,
CNRS, Laboratoire de Physique, F-69342 Lyon, France.**

We study the low frequency admittance of a quantum Hall bar of size much larger than the electronic coherence length. We find that this macroscopic conductor behaves as an ideal quantum conductor with vanishing longitudinal resistance and purely inductive behavior up to $f \lesssim 1$ MHz. Using several measurement configurations, we study the dependence of this inductance on the length of the edge channel and on the integer quantum Hall filling factor. The experimental data are well described by a scattering model for edge magnetoplasmons taking into account effective long range Coulomb interactions within the sample. We find that the inductance's dependence on the filling factor arises predominantly from the effective quantum inertia of charge carriers induced by Coulomb interactions.

PACS numbers: 72.10.-d, 73.23.-b, 73.43.-f, 73.43.Fj

By demonstrating that macroscopic conductors could exhibit robust d.c. transport properties of quantum origin, the integer quantum Hall effect (IQHE) [1–5] has been a major surprise. The importance of this breakthrough for metrology was acknowledged immediately [1] and has led to the redefinition of the Ohm [6]. The finite frequency response of quantum Hall conductors has been intensively studied by metrologists: the use of an a.c. bridge at finite frequency f revealed departure of the Hall resistance $R_H(f)$ at $\nu = 2$ from the expected value $R_K/2 = h/2e^2$ [7–11]. It was then attributed to “intrinsic inductances and capacitances” [12, 13]. Later, Schurr *et al* proposed a double shielded sample allowing for a frequency-independent resistance standard [14], but these works left open the question of the origin of these capacitances and inductances.

On the other hand, the finite frequency transport properties of quantum coherent conductors, of size smaller than the electron coherence length, are expected to be dominated by quantum effects. For low-dimensional conductors such as carbon nanotubes [15], or graphene [16], the inductance is of purely kinetic origin. Small superconducting inductors [17, 18] now used in space industry [19] are based on the inertia of Cooper pairs. For a quantum coherent conductor, the theory developed by Büttiker and his collaborators [20–22] relates the associated L/R or RC times to the Wigner-Smith time delay for charge carriers scattering across the conductor. These remarkable predictions have been confirmed by the measurement of the finite frequency admittance of quantum Hall R-C [23] and R-L [24, 25] circuits of μm -size in the GHz range at cryogenic temperatures.

In this letter, we demonstrate that, in the a.c. regime, a mm long ungated macroscopic quantum Hall bar, of size much larger than the electronic coherence length, exhibits a finite inductance as well as a vanishing longitudinal resistance. Such a purely inductive longitudinal response is expected for quantum conductors with zero backscattering: a kinetic energy cost proportional to the square of the current arises from both the Pauli principle and the linear dispersion relation for electrons close to the Fermi level (see Appendix A). This effective inertia of carriers causes the current response to lag the applied electric field. Here, we identify an inductance of the order of tens of $\mu\text{H mm}^{-1}$ and connect it to an effective velocity v_{eff} along the quantum Hall bar's edges. Contrary to gated samples, in which v_{eff} is almost independent of the filling factor ν [24], we show that, because of Coulomb interactions between opposite edges of the sample, v_{eff} depends on ν in our samples. Using the edge-magnetoplasmon scattering approach combined with a discrete element approach *à la* Büttiker, we show that:

$$\frac{v_{\text{eff}}(\nu)}{v_d(\nu)} = 1 + \frac{\nu\alpha_{\text{eff}}(\nu)}{\pi} \ln \left[\frac{W/\xi_H(\nu)}{\nu} \right] \quad (1)$$

for a sample of width W . Here, $v_d(\nu)$ represents the charge density wave velocity along the system of ν -copropagating chiral edge channels, neglecting Coulomb interactions with the other (counter-propagating) edge channels. In a Büttiker view of the edge channels [26], $v_d(\nu)$ is the drift velocity of non-interacting electrons at the edge in an effective confining potential U_ν and, therefore, it plays the role of an effective Fermi velocity in the 1D linear dispersion relation along the edge [27]. In the presence of compressible stripes, which appear for a sufficiently smooth confining potential [28], it corresponds to the effective velocity of the charge density mode in

* Corresponding Author : christophe.chaubet@umontpellier.fr

the system of ν copropagating edge channels [29], taking into account the presence of the incompressible part of the edge channel [30]. Nevertheless, we denote it by $v_d(\nu)$ because, in a model of an edge channel without compressible parts, it really would be an electronic drift velocity. Importantly, this velocity deviates from the classical $1/B$ behavior of the electronic drift velocity because of screening effects, which change the electrostatic potential at the edge as ν varies.

Here, $\alpha_{\text{eff}}(\nu)$ denotes the effective fine structure constant (α_{qed} in the vacuum) at filling factor ν : $\alpha_{\text{eff}}(\nu) = (\alpha_{\text{qed}}/\epsilon_r) \times (c/v_d(\nu))$. The length $\xi_H(\nu)$, which also depends on ν , is an effective renormalized width of a single edge channel of the order of the width of incompressible edge channels $\lambda_H(\nu)$ [28] (see Appendix D)

Our work demonstrates that the purely inductive response of the macroscopic ungated quantum Hall bar reflects the effective quantum inertia of charge carriers renormalized by Coulomb interactions within the sample. Therefore, although electron transport across such a conductor is not coherent, its d.c. and a.c. transport properties are of quantum origin, a fact that ultimately relies on the coherence of edge-magnetoplasmon (EMP) modes propagating along chiral edge channels. EMP coherence has enabled the demonstration of single and double EMP Fabry-Pérot interferometers [31] as well as of a Mach-Zehnder plasmonic interferometer [32].

Using shallow etching, our samples are processed on an AlGaAs/GaAs heterojunction with the two dimensional electron gas (2DEG) located at the hetero-interface (105 nm beneath the surface) with carrier density $n_s = 5.1 \times 10^{11} \text{ cm}^{-2}$ and mobility $\mu = 30 \text{ m}^2/\text{Vs}$. We have processed a $2 \times 0.4 \text{ mm}^2$ ungated Hall bar which exhibits a sufficiently large kinetic inductance. The sample has no back gate and is glued on a ceramic sample holder to avoid parasitic capacitances. It is placed at the center of a high magnetic field at 1.5 K.

In the measurement setup depicted on Fig. 1-a., the current is injected using H_{cur} (5 mV bias), and measured using L_{cur} . The potential of H_{pot} is measured while $V = 0$ and $I = 0$ are imposed at L_{pot} . The current intensity ($\lesssim 0.5 \mu\text{A}$ at $\nu = 2$) remains below the breakdown current and currents used in metrology [4, 7]. For each values of B , the resistance and the reactance have been measured for 300 values of the frequency f in the range 40 Hz-100 kHz.

Due to chirality of the quantum Hall transport, an ohmic contact wire-bonded to the sample holder and so to a coaxial cable, generates a leakage current through the cable capacitance if the potential does not vanish [35, 36]. This results in a faulty measurement [37, 38]. For this reason, all results presented here have been carried out at integer filling factors, where the longitudinal resistance $R_{xx}(\omega)$ vanishes[39]. Furthermore, only 3 of the ohmic contacts processed on the sample were wire-bonded onto the sample holder as shown on Fig. 1.b. To measure a zero resistance state, the third contact is inserted along the edge connected to the reference potential. In d.c.,

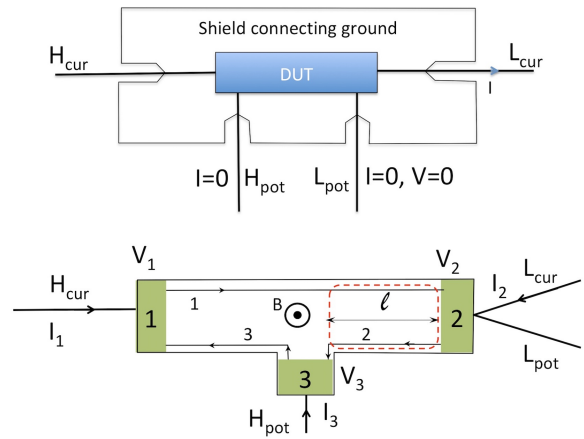


FIG. 1. a) The Device Under Test (DUT) is measured using four coaxial cables and the impedance-meter Agilent HP4294A, which measures the current I at L_{cur} , the potential V at H_{pot} , and gives $G = I/V$, for details see Ref. [33, 34]. Note that the potentials of H_{pot} , L_{pot} , H_{cur} and L_{cur} are the potentials of the four connectors of the impedance-meter. b) Scheme of the multi-terminal Hall bar with only three ohmic contacts wire-bonded onto the sample holder. In this geometry, the impedance is $Z_{23}^{(\text{exp})}(\omega) = -(\partial V_3/\partial I_2)(\omega)$ for $V_2 = 0$.

one would measure a potential $V_{H_{\text{pot}}} = 0$. In a.c., $V_{H_{\text{pot}}} \neq 0$ and we measure the frequency dependent impedance $Z_{23}^{(\text{exp})}(\omega) = -\partial V_3/\partial I_2|_{V_2=0}(\omega)$. Different configurations and edge channel lengths can be obtained by recabling the contacts and changing the sample side (in this case, the magnetic field orientation must be reversed). We have also wire-bonded a fourth ohmic contact on the same side of the sample to connect L_{pot} to access another edge channel length.

Figure 2 presents unfiltered and non-averaged raw data for the reactance $X(f) = \text{Im}(Z_{23}^{(\text{exp})}(2\pi f))$ in a given sample configuration for $\nu = 2, 4, 6$ and 8. The positive linear dependence of $X(f)$ is the signature of an inductive behavior. The corresponding inductance decreases with ν . These data are completely reproducible in the regions of magnetic fields where $R_{xx} = 0$. This is a key point of our work: for integer filling factors, the real part $R(f) = \text{Re}(Z_{23}^{(\text{exp})}(2\pi f))$ of the measured impedance is close to zero with values between $\pm 0.5 \Omega$ at low frequency as shown in the inset of Fig. 2. These results extend the work of Gabelli *et al* [24] in which the sample resistance was $R_H = R_K/\nu$, to the case of a zero resistance macroscopic device. At higher frequencies, a small real part of the measured response function $R(f)$ appears. This effect is discussed in Appendix B and is correlated to the deviation of the reactance $X(f)$ from linearity seen on Fig. 2.

Since the ac transport properties of a quantum Hall conductor is directly related to the scattering of edge-magnetoplasmons [40–42], we have developed an analytical model (see Appendix C) in the spirit of Ref. [31] for scattering of EMP modes in a quantum Hall bar taking

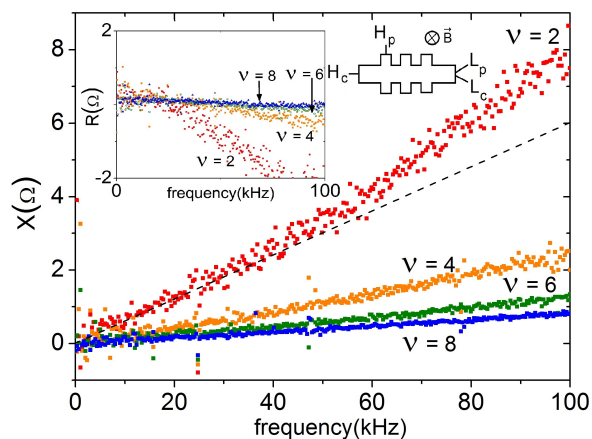


FIG. 2. The reactance $X(f)$ as a function of the frequency f for different ν and $B < 0$, in the measurement configuration shown here. Inset: the longitudinal resistance $R(f)$ vanishes quadratically for integer filling factors at low frequency.

into account long range inter-channel Coulomb interactions. It assumes that, in our ungated quantum Hall bars, all edge channels of same chirality have the same velocity $v_d(\nu)$ and are so strongly coupled that they see the same time dependent potential as in Ref. [25]. Since edge states are distant from more than 1.5 cm from shield of coaxial cables located beneath the sample holder, estimated parasitic capacitance to shield for edge states is below 1 fF while the inter-edge capacitance c_H is of the order of 0.1 pF. Therefore, Coulomb interactions effects are dominated by the inter-edge capacitance C_H . Finally, dissipation of EMP modes have been neglected, an hypothesis a posteriori satisfied in our samples.

In the geometry depicted on Fig. 1, the low frequency expansion of the measured reactance is of the form:

$$\text{Im} \left(Z_{23}^{(\text{exp})}(\omega) \right) = iL\omega + \mathcal{O}(\omega^2) \quad (2)$$

where L denotes the total inductance for the quantum Hall bar delimited by a dashed red box on Fig. 1-b. Because here, the magnetic inductance is much smaller than the kinetic inductance (see Appendix A), L can be obtained from the edge magnetoplasmon scattering model as

$$L = (R_K/\nu) \times (l/2 v_{\text{eff}}(\nu)) \quad (3a)$$

$$v_{\text{eff}}(\nu) = v_d(\nu) \times \left(1 + \frac{C_q(\nu)}{2C_H(\nu)} \right). \quad (3b)$$

where l is the length of the Hall bar (see Fig. 1-b), $C_q(\nu) = \nu e^2 l / \hbar v_d(\nu)$ is the quantum capacitance of ν edge channels and the geometric capacitance $C_H(\nu)$ describes the effect of Coulomb interactions between counter-propagating edge channels. This is different from the quantum RL-circuit where, because of the gating, the capacitance C_H has to be replaced by the capacitance C_g with the nearby gates leading to a renormalization of

v_d by $1 + C_q/C_g$ for right and left moving charge density waves [24]. Here, the renormalization factor involves a C_H capacitance with the series addition $C_q/2$ of the quantum capacitances of counter-propagating edges. As a consequence, Eq. (3) still relates $L = R_H^2 C_\mu$ to the Hall resistance and to the electrochemical capacitance [43] C_μ defined as the series addition of C_H to $C_q/2$. Eq. (3) suggests that the inductance can be interpreted as a kinetic inductance associated with an effective time of flight $l/v_{\text{eff}}(\nu)$. But, as discussed in Appendix C, $v_{\text{eff}}(\nu)$ is neither the drift velocity for non-interacting electrons nor even a renormalized electron's velocity within chiral edge channels, but an effective velocity arising from the combination of their kinetic quantum inertia and Coulomb interactions within the quantum Hall bar. This effective inertia is of quantum origin, reflecting the minimal energy associated with an electrical current and appears, as we will see, to be dominated by the effects of Coulomb interactions.

The geometric capacitance $C_H(\nu)$ depends on the width W of the sample, and of the structure and geometry of the quantum Hall edge channels (see Appendix D), through a length $\xi_H(\nu)$ proportional to the width $W_H(\nu)$ of a single channel. Following Ref. [28], $W_H(\nu) = (1 + \pi^2 \alpha_{\text{eff}}(\nu)) \lambda_H(\nu)$, which is of the order of a few tens of nm for AlGaAs/GaAs quantum Hall systems. Finally, the inter-edge Coulomb interactions contribution to $v_{\text{eff}}(\nu)$

$$\frac{v_d(\nu) C_q(\nu)}{2C_H(\nu)} \simeq \frac{\sigma_H(\nu)}{2\pi\epsilon_0\epsilon_r} \ln \left(\frac{W}{\nu \xi_H(\nu)} \right) \quad (4)$$

is found to be linear in ν , because of its proportionality to the quantum Hall conductivity $\sigma_H(\nu)$, but with a logarithmic multiplicative correction which is a signature of Coulomb interactions.

We will now discuss how this expression and the experimental data enable us to rule out some models for $v_d(\nu)$. We have considered two different models for the confining potential at the edge of the sample which leads to a different prediction for $v_d(\nu)$: in Ref. [44], $v_d(\nu) = \omega_c/k_F$ where $\omega_c = eB/m^*$ is the cyclotron frequency and $k_F = \sqrt{2\pi/n_S}$ the Fermi wave-vector. This leads to a dependance $v_d(\nu) = v_d/\nu$ whereas in Ref. [45], the gradient of the potential is proportional to $\hbar\omega_c/l_B$ where $l_B = \sqrt{\hbar/eB}$ is the magnetic length thereby leading to a scaling $v_d(\nu) = v_d/\sqrt{\nu}$.

Fig. 3 contains the first main quantitative result of this work, *i.e.* the quantum inductance as function of $1/\nu$ for configurations $B < 0$ ($B > 0$ configurations are analyzed in Appendix E). Values have been obtained from the reactance data depicted on Fig. 2 using the slope at low frequency of $f \mapsto X(f)$ datasets. Three configurations in which L_{pot} and H_{pot} are plugged to different contacts (see Fig. 3) and thus correspond to different l have been studied. The main result is the dependence of the inductance on $1/\nu$ which involves a linear part (see Eq. (3a)) due to the presence of ν channels in parallel, but with a non-linear correction stemming from the ν -dependence

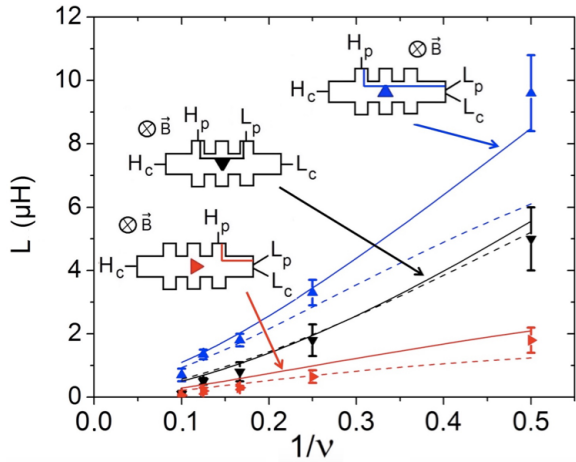


FIG. 3. (Color online) For measurement configurations with $B < 0$ corresponding to $l = 600 \mu\text{m}$, $1000 \mu\text{m}$ and $1600 \mu\text{m}$, the inductance increases with $1/\nu$. Dashed lines correspond to model $v_d(\nu) = v_d/\nu$ with $v_d = 15, 5$ and 40 (in units of 10^5ms^{-1}) from top to bottom. The $v_d(\nu) = v_d/\sqrt{\nu}$ model leads to (solid lines) $v_d = 6, 3$ and 17 in units of 10^5ms^{-1} from top to bottom. The blue points corresponds to the experimental data displayed on Fig. 2.

of $v_d(\nu)$ (see Eqs. (3b)) together with Coulomb interaction effects (see Eq. (4)). The different dependences of $v_d(\nu)$ lead to different theoretical predictions. We find that the scaling $v_d(\nu) = v_d/\sqrt{\nu}$ is the best for describing the experimental data.

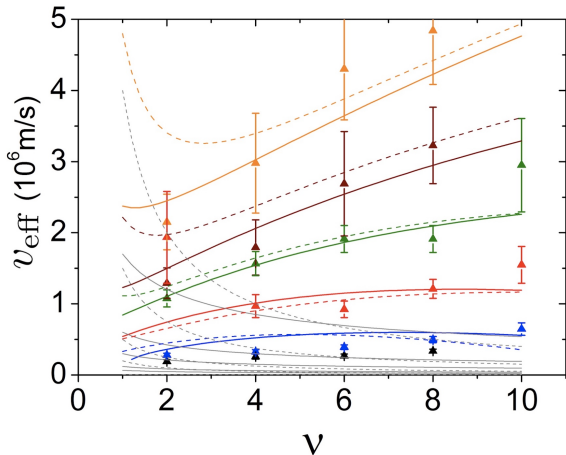


FIG. 4. (Color online) v_{eff} as a function of ν . Dashed curves correspond to $v_d(\nu) = v_d/\nu$ and full lines to $v_d(\nu) = v_d/\sqrt{\nu}$. Colored lines correspond to the expressions (1) taking into account inter-edge Coulomb interactions. Thin grey curves correspond to plots of the bare velocity $v_d(\nu)$. The full lines have been obtained with (starting from the top curve): $v_d = 17$, $v_d = 6$ (fit of the data from Fig. 2), $v_d = 3$, $v_d = 1.2$ and $v_d = 0.66$ in units of 10^5ms^{-1} . For the dashed lines, we have starting from the top curve: $v_d = 40$, $v_d = 15$, $v_d = 5$, $v_d = 2$ and $v_d = 1$ in units of 10^5ms^{-1} .

We have then extracted the velocity $v_{\text{eff}}(\nu)$ using Eq. (3a) from each value of the inductance (see Fig. 4). This is the second main quantitative experimental result of this work. Each family of points corresponds to a specific sample configuration for which the sample has been heated up, re-bonded and cooled down again. These manipulations affect the electrostatic arrangement of charges at the edge, thereby modifying v_d from one experiment to the other. Fig. 4 presents predictions for $v_{\text{eff}}(\nu)$ from Eq. (1) for different models for $v_d(\nu)$. Similarly to the discussion of Fig. 3, the $\nu^{-1/2}$ scaling for $v_d(\nu)$ gives the best reproduction of the experimental data. But a striking point is that in order to reproduce the experimental data, it is necessary to take into account the inter-channel Coulomb interactions: ignoring the interactions would correspond to using $v_d(\nu)$ instead of v_{eff} in Eq. (3a). This is shown by the thin filled and dashed grey curves on Fig. 4, which clearly do not follow the experimental data. We thus interpret the ν -dependence of $v_{\text{eff}}(\nu)$ when increasing ν from 2 to 10 (mostly linear with log-correction) as a strong indication of the dominant role of Coulomb interactions in these ungated samples.

Let us comment on the spread of values for v_d given in Fig. 4, which reflects the variability of the electrostatic environment in the samples from one experimental cooldown to another. A variation by a factor 25 is observed across all experiments (three higher curves for $B > 0$, all others for $B < 0$) but by only a factor 6 when considering only one orientation of B . This is still much larger than the relative change of the 2DEG density but v_d reflects the edge potential, which may vary more from one experiment to the other. As we use a shallow etching technique, the samples edges are very sensitive to any change of the electric potential landscape[46]. The values that we have obtained for $v_d(\nu = 2)$ are compatible with estimates in the literature [47] for shallow etched samples. Moreover, our measurements of $v_{\text{eff}}(\nu)$ are in the same range and qualitatively show a similar ν -dependence as the ones obtained in Ref. [48] for ungated samples by a time-of-flight technique.

To summarize, we have shown that, at low frequencies, a macroscopic quantum Hall bar is a perfect 1D conductor exhibiting a vanishing longitudinal resistance and a finite inductance. By fitting its dependence on ν and on the sample geometry using a simple long range effective Coulomb interaction model in the spirit of Büttiker *et al* [43], we have shown that it reflects the effective quantum inertia of charge carriers within the edges of the quantum Hall bar. Contrary to the case of superconductors where carrier inertia arises from the effective mass of the Cooper pairs, here it reflects how Coulomb interactions alter the propagation of low-frequency massless edge-magnetoplasmon modes. Remarkably, the experimental data can be understood using a simple model which is formally similar to the one used for gated nanofabricated samples [49, 50]: starting from chiral charge transport with bare velocity $v_d(\nu)$, we include Coulomb interactions with the other edges via classical electrostat-

ics and edge structure geometry from Ref. [28]. Going beyond this phenomenological but practical model would involve a multiscale treatment combining our approach to inter-channel interactions with a self-consistent microscopic approach solving the problem of electrons in the presence of intra-channel Coulomb interactions [51–53].

Finally, macroscopic samples may provide a rescaled test-bed for studying the scattering properties of edge-magnetoplasmons in 1 to 100 μm -sized samples. Studying a.c. transport properties of macroscopic samples up to radio-frequencies could thus open the way to realizing controlled quantum linear components for quantum nano-electronics in 1D edge channels, with possible applications to electron [54] and micro-wave quantum optics in ballistic quantum conductors [55].

ACKNOWLEDGMENTS

We warmly thank G. Fève, Ch. Flindt and B. Plaçais for useful discussions and suggestions as well as the referees for important comments and clarifications on this manuscript. This work has been partly supported by ANR grant “1shot reloaded” (ANR-14-CE32-0017) and the French Renatech network.

Appendix A: Kinetic and magnetic inductance

In this section, we compare the kinetic inductance of a quantum Hall bar at filling fraction ν to its geometric inductance.

1. Kinetic inductance

Let us first consider non-interacting chiral charge carriers with propagation velocity v_d (see Fig. 5). As explained in the main text, for incompressible quantum Hall edge channels, this velocity is a drift velocity $v_d(\nu) = -\partial_y U_\nu / B$ which depend on ν via the magnetic field and the dependence of the confining potential U_ν on ν itself as will be detailed in Sec. D2. However, to keep notations simple, we shall denote it by v_d instead of $v_d(\nu)$ unless necessary.

A net current flow corresponds to a chemical potential imbalance between chiral edge channels of opposite chirality. The corresponding kinetic energy is then obtained by adding together the energy of all quantum states which have been occupied when biasing chiral edge states with different chemical potential $\Delta\mu = -eV$:

$$E_{\text{chir}} = \sum_k \varepsilon(k) = \nu \times g(\varepsilon) l \times (eV)^2 / 2, \quad (\text{A1})$$

where $g(\varepsilon) = 1/hv_d$ is the density of states (DOS) per unit length for a 1D-channel, ν the number of channels, l the edge-state length. The voltage drop across

the sample is $V = R_H I_\nu$, where $R_H = R_K / \nu = h/e^2 \nu$ denotes the quantum Hall resistance at filling fraction ν and I_ν the current. The resulting kinetic energy is then quadratic in the current, as expected for a linear inductor:

$$E_{\text{chir}}(I_\nu) = \frac{\nu e^2}{hv_d} \times \frac{l}{2} \times \left(\frac{R_K I_\nu}{\nu} \right)^2 = \frac{h}{e^2} \times \frac{l}{\nu v_d} \times \frac{I_\nu^2}{2}. \quad (\text{A2})$$

For a quantum Hall bar, we have two counter-propagating groups of ν chiral edge channels. Assuming that the two chiralities carry equal charge of the total current $I_\nu = \pm I/2$, this leads to a total kinetic energy

$$E_K(I) = 2E_{\text{chir}}(I/2) = \frac{h}{e^2} \times \frac{l}{\nu v_d} \times \frac{2(I/2)^2}{2}. \quad (\text{A3})$$

Using $E_K(I) = LI^2/2$, we obtain the following formula for the inductance L of the quantum Hall bar:

$$L = \frac{R_K}{\nu} \times \frac{l}{2v_d(\nu)} \quad (\text{A4})$$

Note the appearance of the half of the time of flight $l/v_d(\nu)$ of the electrons across the quantum Hall bar which is ultimately due to the existence of two counter-propagating groups of copropagating edge channels.

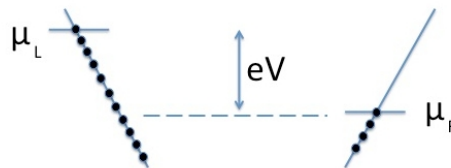


FIG. 5. Dispersion relations for non-interacting electrons propagating along a right-moving chiral edge channel R and a left moving one L with propagation velocity $\pm v_d$. In the presence of a d.c. voltage bias V , a chemical potential imbalance $-eV$ appears between the two chiral edge channels. At filling fraction ν , such a bias generates a net current $I = (e^2 \nu / h) \times V$.

2. Magnetic inductance

A quantum Hall bar can be viewed as a conductor built from two linear wires of length l , and of diameter or width W_H separated by a distance W which is the width of the quantum Hall bar. The magnetic inductance of the resulting dipole can be computed from Biot-Savart’s law [56]. Note that the wire’s diameter $W_H(\nu)$ usually scales as ν (see Ref. [28] and Sec. D1). In the quantum Hall bar geometry, the total current I flowing across the quantum Hall bar corresponds to $\pm I/2$ along each of the two long counter-propagating edges. Consequently, in the limit $l, W \gg W_H(\nu)$, the geometric inductance of the quantum Hall bar is approximately equal to

$$L_m = \frac{l\mu}{\pi} \left[\ln \left(\frac{2W}{W_H(\nu)} \right) - 1 \right] \quad (\text{A5})$$

where $\mu = \mu_r \mu_0$ is the magnetic permeability of the material expressed as the product of its relative permeability μ_r by the vacuum permittivity $\mu_0 = 1/\varepsilon_0 c^2$. For a non-magnetic material such as AlGaAs/GaAs, $\mu_r = 1$ and therefore $\mu = \mu_0$.

Using this expression and Eq. (A4), the ratio of the magnetic to the kinetic inductance is given by:

$$\frac{L_m}{L_K} = 4\alpha_{\text{qed}} \frac{v_d}{c} \times \nu \times \left[\ln \left(\frac{2W}{W_H(\nu)} \right) - 1 \right] \quad (\text{A6})$$

where α_{qed} is the fine structure constant. The magnetic character of this ratio appears through the multiplication factor $v_d/c \ll 1$. Together with the smallness of α_{qed} and the logarithmic dependence in the aspect ratio $W/W_H(\nu) \sim W/\nu W_H(1)$, this explains why the magnetic inductance is always much smaller than the kinetic one for $\nu \lesssim 100$.

Appendix B: Experimental signals

In this section, we discuss how the quantities that are measured in the experiment are related to the a.c. response of a quantum Hall bar even in the presence of experimental imperfections such as cable capacitances.

1. Finite frequency transport in quantum Hall edge channels

In his pioneering work on finite frequency charge transport in mesoscopic conductors [20], Büttiker stressed the importance of interactions: time dependent drives applied to reservoirs lead to charge pumping in the conductor which, in return, alter the electrical potential within the conductor. As a result, its transport properties can no longer be derived by using the d.c. response at zero bias. Büttiker then developed a self consistent mean-field approach to this problem, taking into account how the time dependent charge density within the conductor generates a time-dependent potential and thereby alters the transport [22]. In the linear regime, the a.c. response of the conductor is described by the admittance matrix

$$G_{\alpha\beta}(\omega) = \left. \frac{\partial I_\alpha(\omega)}{\partial V_\beta} \right|_{V=0} \quad (\text{B1})$$

giving the average current entering the conductor from lead α when a voltage drive at the same frequency $\omega/2\pi$ is applied to the reservoir β . Charge conservation and gauge invariance imply that the finite frequency admittance matrix satisfy the general sum rules

$$\sum_{\alpha} G_{\alpha\beta}(\omega) = 0 \quad (\text{B2a})$$

$$\sum_{\beta} G_{\alpha\beta}(\omega) = 0 \quad (\text{B2b})$$

which is ensured by total screening of effective Coulomb interactions.

At low frequency, this admittance matrix is expanded in ω , the zero-th order term being its d.c. conductance $G_{\alpha\beta}^{(\text{dc})}$. The first order term is related to the emittances introduced by Büttiker *et al.* :

$$G_{\alpha\beta}(\omega) = G_{\alpha\beta}^{(\text{dc})} - i\omega E_{\alpha\beta} + \mathcal{O}(\omega^2). \quad (\text{B3})$$

For quantum Hall edge channels, Christen and Büttiker [43] fully exploited the chirality of charge transport to compute the dc conductances $G_{\alpha\beta}^{(\text{dc})}$ as well as the emittances $E_{\alpha\beta}$ using a discrete element description of the circuit.

Here we will show how to describe the finite frequency transport using the building blocks of a discrete element description of quantum Hall bars and the finite frequency admittance properties obtained from the edge-magnetoplasmon (EMP) scattering approach. The details of how the admittances are obtained from the EMP scattering approach are described in Sec. C.

Depending on the sign of the diagonal emittances, the quantum conductor under consideration exhibits a capacitive ($E_{\alpha\alpha} > 0$) or inductive ($E_{\alpha\alpha} < 0$) behavior. Basic examples of these behaviors, involving two different two-contact devices, have been given by Christen and Büttiker [43]. A two-contact Hall bar is predicted to act as an inductance while a ring shaped sample (the so-called Corbino geometry) acts as a capacitance. Hence both geometries exhibit opposite diagonal emittances, which can be understood in terms of reaction of the circuit to an injected charge. Indeed, as shown on Fig. 1 of [43] a charge injected by contact 1 into a Hall bar is transmitted to contact 2, while the charge induced by inter-edge Coulomb interactions created at contact 2 is transmitted to contact 1. On the contrary, in a Corbino sample, the injected charge returns to the contact it comes from, as does the image charge. It was experimentally shown by Delgard *et al.* [57] that Corbino emittances will exhibit this predicted capacitive behavior. Here, we will highlight the inductive behavior of quantum Hall bars in a multi-contact geometry that ensures vanishing longitudinal resistance.

We shall now discuss how, for two different sample configurations, the measured response function relates to the finite frequency admittance of the quantum Hall bar depicted as a red dashed rectangle in the two forthcoming figures, taking into account capacitive leaks at the contacts.

2. Three contact geometry

Let us first consider the three contact geometry depicted on Fig. 6. Contacts 1 and 2 are directly connected to reservoirs whereas contact 3 is not but we take into account the cable capacitance C_0 of the cable. In this section, we shall compute the experimentally measured

finite frequency impedance

$$Z_{23}^{(\text{exp})}(\omega) = - \left. \frac{\partial V_3(\omega)}{\partial I_2(\omega)} \right|_{V_2=0} \quad (\text{B4})$$

up to second order in ω and show how it relates to the properties of the quantum Hall bar B and to the cable capacitance C_0 (see Fig. 6).

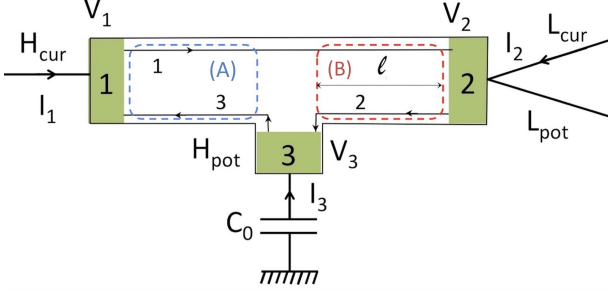


FIG. 6. The device under test when three Ohmic contacts are wire-bonded onto the sample holder. The quantum Hall bar B , which is the dipole under test, is shown as a dashed red box. The quantum Hall bar A is shown as a dotted blue box. The capacitance of the coaxial cable connected to contact 3 is denoted by C_0 . In this experimental setup, $V_2 = 0$ whereas the drive V_1 is non zero and the experimentally measured impedance is $Z_{23}^{(\text{exp})} = -\partial V_3/\partial I_2$.

a. Obtaining $Z_{23}^{(\text{exp})}$

In this approach, the quantum Hall bars A and B delimited on Fig. 6 are characterized by their frequency-dependent EMP scattering matrix. For the quantum Hall bar A , the EMP scattering matrix, which we denote here by $\mathbf{A}(\omega)$ relates the ingoing and outgoing currents through [58]

$$\mathbf{j}^{(\text{out})}(\omega) = \mathbf{A}(\omega)\mathbf{j}^{(\text{in})}(\omega) \quad (\text{B5})$$

in which the edges of the Hall bar are labeled by their chirality. In the same way, the EMP scattering matrix of the quantum Hall bar B will be denoted by $\mathbf{B}(\omega)$. These matrices are computed in Sec. C but for the moment, we won't need their explicit form.

At contact 3, the incoming and outgoing currents propagating within the edge channels are also related by an input/output relation that reflects the time delay associated with the $R_H C_0$ relaxation time of the contact:

$$i_{3,\text{out}}(\omega) = \frac{i_{3,\text{in}}(\omega)}{1 - iR_H C_0 \omega} \quad (\text{B6})$$

Eliminating the edge channel currents internal to the sample directly leads to the finite frequency admittances connecting the currents I_α entering from the reservoirs to the drive voltage V_1 :

$$R_H I_2 = - \frac{A_{RR} B_{RR}}{1 - A_{RL} \mathcal{T} B_{LR}} V_1 \quad (\text{B7})$$

in which the matrix elements of the Hall bar's current scattering matrices \mathbf{A} and \mathbf{B} are involved as well as $\mathcal{T}(\omega) = 1/(1 - iR_H C_0 \omega)$, the edge current transmission of the Ohmic contact with cable capacitance C_0 . For simplicity, the ω dependence of V_1 , I_2 and of the scattering matrix elements of the A and B quantum Hall bars as well as of \mathcal{T} have been omitted. The potential of the contact 3 can also be computed as

$$-i\omega C_0 R_H V_3 = \frac{(\mathcal{T} - 1) B_{LR} A_{RR}}{1 - A_{RL} \mathcal{T} B_{LR}} V_1 \quad (\text{B8})$$

which finally leads to

$$\frac{Z_{23}^{(\text{exp})}(\omega)}{R_H} = \frac{1}{1 - iR_H C_0 \omega} \frac{B_{LR}(\omega)}{B_{RR}(\omega)}. \quad (\text{B9})$$

Note that, at low frequency ($\omega R_H C_0 \ll 1$), the result only depends on the finite frequency properties of the B quantum Hall bar *i.e.* the dipole under test in this setting.

b. Effect of the finite frequency deviation of $\text{Re}(Z_{xy}(\omega))$ from R_H on $Z_{23}^{(\text{exp})}$

It is then useful to relate $Z_{2,3}^{(\text{exp})}$ to the impedance of the Hall bar B , which we know has a real part $\sim R_H$, with a small deviation for $\omega \neq 0$, as observed by metrologists studying the quantum Hall resistance at low frequencies [15-17].

This is achieved using the relation [41, 59] between the quantum Hall bar finite admittance matrix and its edge-magnetoplasmon scattering matrix to obtain the following expression, valid when the left and right moving edges of the quantum Hall bar are in total mutual influence:

$$\frac{Z_{23}^{(\text{exp})}(\omega)}{R_H} = \frac{z_H(\omega) - 1}{1 - iR_H C_0 \omega} \quad (\text{B10})$$

in which $z_H(\omega)$ denotes the dimensionless impedance of the quantum Hall bar B in units of R_H . Note that within the framework of the edge-magnetoplasmon scattering model presented in Sec. C, $z_H(\omega) = 2Z(\omega)/R_H$ where $Z(\omega)$ is given in terms of the edge-magnetoplasmon scattering matrix by Eq. (C15b). It thus predicts $\text{Re}(z_H(\omega)) = 1$ and therefore $\text{Re}(Z_{23}^{(\text{exp})}(\omega)) = 0$.

However, we will now show that a non vanishing $r(\omega) = \text{Re}(z_H(\omega)) - 1$ is responsible for the non-linearity of $X(f)$ seen on Fig. 2 of the paper. Such a feature has been observed for long time by metrologists studying quantum Hall resistance at low frequencies [7, 10, 11]. In the metrology community, this finite frequency deviation $r(\omega)$ from the dc quantum Hall value is commonly attributed to parasitic effects such as self and resistance of ohmic contacts and bond wires and thus depend on configurations and samples. A quadratic dependence on the frequency is usually found in the form $r(\omega) = a_2(\omega/2\pi)^2$.

The a_2 parameter has been measured in many configurations and samples and has been found to be positive or negative but is always around (or below) 10^{-7} /kHz² [7, 10, 11].

To discuss the experimental results, which include both the real and imaginary parts of $Z_{23}^{(\text{exp})}(\omega)$, let us therefore write

$$z_H(\omega) = 1 + r(\omega) + i\omega\tau_H(\omega) \quad (\text{B11})$$

in which $r(\omega)$ denotes the frequency-dependent deviation to R_H (when non zero), and $\tau_H(\omega) = L_{\text{eff}}(\omega)/R_H$ is the dimensionless frequency-dependent effective RL -time of the quantum Hall bar ($L = L_{\text{eff}}(\omega = 0)$). The low frequency expansion of the experimentally measured impedance $Z_{23}^{(\text{exp})}(\omega)/R_H$ is then

$$\frac{Z_{23}^{(\text{exp})}(\omega)}{R_H} \simeq r(\omega) - \omega^2 L_{\text{eff}}(\omega) C_0 \quad (\text{B12a})$$

$$+ i\omega \left[\frac{L_{\text{eff}}(\omega)}{R_H} + R_H C_0 r(\omega) \right] + \mathcal{O}(\omega^3) \quad (\text{B12b})$$

In our experiments, the reactance $\text{Im} \left(Z_{23}^{(\text{exp})}(\omega) \right)$ is obviously dominated by the kinetic inductance L :

$$\text{Im} \left(Z_{23}^{(\text{exp})}(\omega) \right) = \omega L, \quad (\text{B13})$$

but $r(\omega)$ is seen through the deviations of the imaginary part from linearity (see Fig. 2 of the paper). It is nevertheless small and therefore, the dominant contribution to the real part $\text{Re} \left(Z_{23}^{(\text{exp})}(\omega) \right)$ is a negative quadratic one directly proportional to the cable capacitance: $-\omega^2 LC_0$, as observed in the inset of Fig. 2 of the paper.

Both real and imaginary part of admittance seen in Fig. 2 suggest a quadratic behavior for $r(\omega)$. To second order in $\omega R_K C_0$:

$$\text{Re} \left(\frac{Z_{23}^{(\text{exp})}(\omega)}{R_H} \right) = (R_H C_0 \omega)^2 \left[r_2 - \frac{L/R_H}{R_H C_0} \right] \quad (\text{B14})$$

where $r(\omega) \simeq r_2 (\omega R_H C_0)^2$.

In our experiments, the cable capacitance is $C_0 = 218$ pF. We deduce from Fig. 2 of the paper that, at $\nu = 2$ and $\omega/2\pi = 100$ kHz, $\omega r(\omega) R_H^2 C_0 \approx 2.2 \Omega$. This gives $r(\omega) \approx 10^{-4}$ at 100 kHz thereby corresponding to $a_2 = 4\pi^2 r_2 (R_H C_0)^2 \approx 10^{-8}$ /kHz², a value in total agreement with the deviations reported in the literature. Consequently, the observed deviations from pure inductive behavior can be explained by the combined effect of the cable capacitance and of the deviations of $\text{Re}(Z_H(\omega))$ from its dc value R_H .

3. Four contact geometry (two on the same side)

Let us now turn to the case of a four contact sample depicted on Fig. 7. This geometry represent a four contact

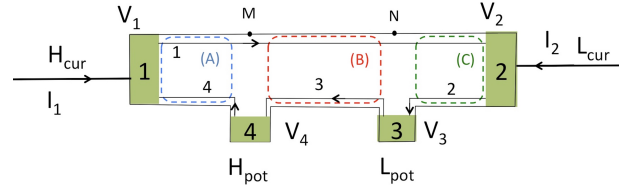


FIG. 7. The device under test has now four contacts connected to sample holder, two of them being on same side. The quantum Hall bar is divided into three parts, shown as colored box, A (blue), B (red) and C (green). H_{pot} and L_{pot} are connected respectively to contacts 4 and 3. In this configuration, the low frequency impedance depends only on the central Hall bar B.

measurement of the central part B of the device. Here, the parts A and C of the device play the role of the leads that connect B to the current injection reservoirs which are the Ohmic contacts 1 and 2. The Ohmic contacts 3 and 4 are used for measuring the voltage difference between the two port of the would-be dipole B .

In this section, the capacitances C_0 of the cables will be omitted for simplicity. This does not change the physics of the problem but greatly simplifies the computations. Nonetheless, we know from Eq. (B6) that the same prefactor $(1 - iR_H C_0 \omega)^{-1}$ will appear in the results when capacitances are taken into account.

We assume that A , B and C can be modeled as quantum Hall bars characterized by their edge-magnetoplasmon scattering matrices. Exactly as before, this amounts to neglecting Coulomb interactions outside the Hall bars themselves, an hypothesis consistent with the total screening hypothesis stated in Sec. C 1. Let us denote by M and N the points on edge channel 1, which respectively face contacts 4 and 3. Introducing the EMP scattering matrices \mathbf{A} , \mathbf{B} and \mathbf{C} respectively associated with the three quantum Hall bars A , B and C represented on Fig. 7, the dynamics of the three quantum Hall bars is described by:

$$\begin{pmatrix} i_M \\ i_{4,\text{out}} \end{pmatrix} = \mathbf{A} \begin{pmatrix} i_{1,\text{in}} \\ i_{4,\text{in}} \end{pmatrix} \quad (\text{B15a})$$

$$\begin{pmatrix} i_N \\ i_{3,\text{out}} \end{pmatrix} = \mathbf{B} \begin{pmatrix} i_M \\ i_{3,\text{in}} \end{pmatrix} \quad (\text{B15b})$$

$$\begin{pmatrix} i_{1,\text{out}} \\ i_{2,\text{out}} \end{pmatrix} = \mathbf{C} \begin{pmatrix} i_N \\ i_{2,\text{in}} \end{pmatrix} \quad (\text{B15c})$$

in which, for compactness, the ω dependence is not recalled. In the experimental configuration depicted in Fig. 7, $V_3 = 0$ and we measure V_4 . We calculate I_2 and V_4 , in order to find $Z_{42}^{(\text{exp})} = V_4/I_2$. The lead potentials fix the incoming currents injected by the reservoirs. Moreover, because of the high impedance of the voltmeter connected to H_{pot} and L_{pot} , we neglect the currents leaking

into these Ohmic contacts. We thus have:

$$i_{1,\text{in}} = G_H V_1, \quad i_{2,\text{in}} = G_H V_2 \quad (\text{B16a})$$

$$i_{3,\text{in}} = 0, \quad i_{4,\text{in}} = G_H V_4 \quad (\text{B16b})$$

$$i_{3,\text{in}} = i_{2,\text{out}}, \quad i_{4,\text{in}} = i_{3,\text{out}} \quad (\text{B16c})$$

$$I_2 = i_{2,\text{in}} - i_{1,\text{out}}. \quad (\text{B16d})$$

From Eqs. (B15a) and (B15b), we obtain :

$$\begin{aligned} G_H V_4 &= i_{4,\text{in}} = i_{3,\text{out}} \\ i_{3,\text{out}} &= B_{LR}(A_{RR}G_H V_1 + A_{RL}G_H V_4) \end{aligned} \quad (\text{B17})$$

or, equivalently:

$$V_4 = \frac{B_{LR}A_{RR}}{1 - B_{LR}A_{RL}} V_1. \quad (\text{B18})$$

On the other hand, calculating I_2 :

$$I_2 = G_H V_2 - i_{2,\text{out}} = G_H V_2(1 - C_{RL}) - C_{RR}i_N, \quad (\text{B19})$$

using now Eq. (B15c), this becomes a current division relation $I_2 = \mathcal{C} i_N$ where

$$\mathcal{C} = \frac{-C_{RR}C_{LL} - C_{LR} + C_{LR}C_{RL}}{C_{LL}}. \quad (\text{B20})$$

Eqs. (B15a) to (B15b) then shows that $i_N = B_{RR}i_M$. We now use Eq. (B15a) to express i_M in terms of $G_H V_1$ and $G_H V_4$. Using Eq. (B18), we obtain :

$$i_N = \left(\frac{B_{RR}A_{RR}}{1 - B_{LR}A_{RL}} \right) G_H V_1. \quad (\text{B21})$$

This gives us the total current entering lead 2 in terms of the applied voltage V_1 at the right Ohmic contact:

$$I_2 = \mathcal{C} \frac{B_{RR}A_{RR}}{1 - B_{LR}A_{RL}} G_H V_1 \quad (\text{B22})$$

Using one last time the voltage division relation (B18), the dimensionless impedance $z_{24} = Z_{24}^{(\text{exp})}/R_H = G_H V_4/I_2$ is thus finally given by:

$$z_{24} = \frac{B_{LR}}{B_{RR} \times \mathcal{C}}. \quad (\text{B23})$$

As in the three contact case, the fraction B_{LR}/B_{RR} appears in the results showing that the four point measurement does give us information on the B quantum Hall bar. However, the matrix C is involved via the quantity \mathcal{C} . Nevertheless, it is possible to show that, to the lowest order frequency expansion, z_{24} does not depend on the physical relevant information contained within the C matrix. For this we once again use the low frequency expansion of the C scattering matrix (see Eq. (C12)):

$$C_{LL} = C_{RR} = 1 + C_{RL} \quad (\text{B24})$$

$$C_{LR} = C_{RL} = \frac{-i\omega l_C}{v_d(2 + \nu\alpha_\nu)} = -i\omega\tau_C \quad (\text{B25})$$



FIG. 8. A simple quantum Hall bar at filling fraction $\nu = 3$ connecting the G lead to the D lead. Along the R edge channels, electrons are right movers flowing from lead G to lead D whereas for edge channels L , they are left movers.

where l_C is the length of Hall bar C , and $\tau_C = \frac{l_C}{2v_d(1+\nu\alpha_\nu/2)}$ is the transit time across the Hall bar C . These formulas allow the calculation of quantity \mathcal{C} from its definition by Eq. (B20) at the first order in $\omega\tau_C$:

$$\mathcal{C} = -1 + 2i\omega\tau_C + o((\omega\tau_C)^2). \quad (\text{B26})$$

Finally, using Eq. (B23),

$$z_{24} = \frac{-i\omega\tau_B}{(1 - i\omega\tau_B)(-1 + 2i\omega\tau_C)} \simeq i\omega\tau_B + o((\omega\tau_C)^2) \quad (\text{B27})$$

showing that the measured inductance corresponds to the transit time in Hall bar B . Thus, the length involved in the determination of velocities is $l = l_B$.

Appendix C: Discrete element description from edge-magnetoplasmon scattering

In this Section, we present the computation of the EMP scattering matrix for an ungated quantum Hall bar and derive the corresponding description in terms of discrete elements valid at low frequency.

1. The model

We consider a quantum Hall bar of length l in the integer quantum Hall regime with filling fraction $\nu \geq 1$ as depicted on Fig. 8. We denote by R (resp. L) the upper (resp. lower) edge channels which are right (resp. left) movers as depicted on Fig. 8. We denote by $j_\alpha^{(\text{in})}$ the incoming current entering the Hall bar on side $\alpha = R, L$ and $j_\alpha^{(\text{out})}$ the outgoing one. Our goal is to relate the outgoing currents to the incoming ones in the presence of Coulomb interactions.

Here v_d denotes the charge transport velocity, which for simplicity we take identical for all chiral edge channels. Coulomb interactions are described by assuming a discrete element model *à la* Christen-Büttiker [43] in which all the electrons within channels of the same chirality see the same time dependent potential $U_R(t)$ (for

right movers) and $U_L(t)$ (for left movers). These potentials are related to the total charge stored within the L and R edge channels by a capacitance matrix

$$\mathbf{Q} = \mathbf{C} \mathbf{U} \quad (\text{C1})$$

in which

$$\mathbf{Q} = \begin{pmatrix} Q_R \\ Q_L \end{pmatrix}, \quad \mathbf{U} = \begin{pmatrix} U_R \\ U_L \end{pmatrix} \quad (\text{C2})$$

and \mathbf{C} denotes the capacitance matrix

$$\mathbf{C} = \begin{pmatrix} C_H & -\eta C_H \\ -\eta C_H & C_H \end{pmatrix}, \quad (\text{C3})$$

where $0 \leq \eta \leq 1$ depending on the screening of Coulomb interaction between channels of opposite chiralities by nearby gates and other on-chip conductors. Eq. (C1) plays the role of a solution of the Poisson equation relating the electrical potential to the charge density. In this work, unless otherwise stated, we assume that the left and right chiral edge channels are in total influence and therefore that $\eta = 1$. The capacitance C_H can then be computed as the geometric capacitance of a stripline capacitor (see Sec. D).

The charges within the edge channels are directly related to the incoming and outgoing currents through charge conservation which, in the Fourier domain and in vector notation, is written as

$$\mathbf{j}^{(\text{in})}(\omega) - \mathbf{j}^{(\text{out})}(\omega) = -i\omega \mathbf{Q}(\omega). \quad (\text{C4})$$

The last equation we need is the equation of motion for the charge or current density within the Hall bar [60]:

$$\mathbf{Q}(\omega) + C_q(l, \nu; \omega) \mathbf{U}(\omega) = \frac{l}{v_d} f\left(\frac{\omega l}{v_d}\right) \mathbf{j}^{(\text{in})}(\omega), \quad (\text{C5})$$

in which $f(x) = (e^{ix} - 1)/ix$, and

$$C_q(l, \nu; \omega) = \frac{\nu e^2 l}{\hbar v_d} f\left(\frac{\omega l}{v_d}\right) \quad (\text{C6})$$

represents the effective quantum capacitance at frequency $\omega/2\pi$ for the edge channels of length l and filling fraction ν . Eq. (C5) expresses that the charge stored within each edge channels comes from what is injected by the reservoirs and from the shift of the bottom of the electronic bands by the electric potential seen by all electrons.

2. Edge magnetoplasmon scattering

Using Eqs. (C1) and (C4) to eliminate $\mathbf{Q}(\omega)$ and $\mathbf{U}(\omega)$ from Eq. (C5) leads to

$$(C_q(l, \nu; \omega) + \mathbf{C}) \mathbf{j}^{(\text{out})}(\omega) = (C_q(l, \nu; \omega) + e^{i\omega l/v_d} \mathbf{C}) \mathbf{j}^{(\text{in})}(\omega). \quad (\text{C7})$$

Solving this equation leads to the scattering matrix $S(\omega)$ relating incoming to outgoing electrical currents at ω . From the bosonization point of view, this is the scattering matrix for the bosonic counter-propagating edge-magnetoplasmon modes carrying the total charges of the ν right and ν left moving edge channels.

This scattering matrix depends on a dimensionless coupling constant α_ν characterizing the strength of Coulomb interactions within each edge channel by the way of the ratio of the bare quantum capacitance of a single edge channel with drift velocity v_d to the geometric capacitance [61]:

$$\alpha_\nu = \frac{C_q(l, \nu; \omega = 0)}{C_H(l)\nu} = \frac{e^2 l / \hbar v_d(\nu)}{C_H(l)}. \quad (\text{C8})$$

The higher this number, the higher is Coulomb's energy $e^2/C_H(l)$ with respect to the kinetic energy scale $\hbar v_d/l$. The geometric capacitance can be evaluated using standard electrostatics as explained in Sec. D. The result comes under the form

$$C_H(l) = \varepsilon_0 \varepsilon_r l f_{\text{bar}}(W, W_H(\nu)) \quad (\text{C9})$$

in which ε_r is the relative permittivity of the material and $f_{\text{bar}}(W, W_H(\nu))$ is a geometrical factor that depends on the width W of the quantum Hall bar and on $W_H(\nu)$, the width of the system of ν copropagating edge channels at the edge of the quantum Hall bar. The latter is proportional to the filling fraction ν and, in the $W_H(\nu) \ll W$ limit, the geometric factor f_{bar} depends logarithmically on the aspect ratio $W/W_H(\nu)$ as shown in Sec. D. The dimensionless coupling constant

$$\alpha_\nu = \frac{2 \alpha_{\text{eff}}(\nu)}{f_{\text{bar}}(W, W_H(\nu))} \quad (\text{C10})$$

is therefore proportional to the effective fine structure constant at filling fraction ν

$$\alpha_{\text{eff}}(\nu) = \frac{e^2}{4\pi \varepsilon_r \varepsilon_0 \hbar v_d(\nu)} = \frac{\alpha_{\text{qed}}}{\varepsilon_r} \frac{c}{v_d(\nu)}. \quad (\text{C11})$$

up to a subdominant logarithmic dependence in ν arising from classical electrostatics (see Sec. D). The ω dependence is an $X = \omega l/v_d$ dependence involving the free electron time of flight l/v_d along the edges of the quantum Hall bar. Solving Eq. (C7) leads to the edge magnetoplasmon scattering amplitudes

$$S_{RL}(\omega) = S_{LR}(\omega) = \frac{-iX f(X)}{2 + \nu \alpha_\nu f(X)} \quad (\text{C12a})$$

$$S_{RR}(\omega) = S_{LL}(\omega) = 1 - S_{RL}(\omega). \quad (\text{C12b})$$

Note that the relation between diagonal and off diagonal S matrix elements given by Eq. (C12b) is only valid for total screening ($\eta = 1$). One should also note that because of the symmetric setup considered here, the edge magnetoplasmon scattering matrix is determined by its diagonal coefficient $S_d(\omega) = S_{RR}(\omega) = S_{LL}(\omega)$ and

its off-diagonal coefficient $S_{\text{od}}(\omega) = S_{LR}(\omega) = S_{RL}(\omega)$. They satisfy the unitarity conditions

$$|S_{\text{d}}(\omega)|^2 + |S_{\text{od}}(\omega)|^2 = 1 \quad (\text{C13a})$$

$$\text{Re}(S_{\text{d}}(\omega)S_{\text{od}}(\omega)^*) = 0. \quad (\text{C13b})$$

which ensure energy conservation within the quantum Hall bar.

3. Finite frequency impedances

In the spirit of Büttiker, let us derive a discrete element circuit description of the quantum Hall bar. In full generality, this description involves a three terminal circuit in order to take into account the electrostatic coupling to external gates which are assumed to be at the ground here (see Fig. 9). In our experimental, ungated samples, this coupling is expected to be small as we shall see. Note that the symmetry of the Hall bar under magnetic field reversal justifies considering two identical impedances $Z(\omega)$ on both sides of the central node A on Fig. 9. For this tri-terminal circuit, one can combine the relation between the potentials V_G, V_D, V_A and $V_0 = 0$ (by gauge invariance) and the current sum rule $I_G + I_D + I_0 = 0$ to relate I_G and I_D to V_G and V_D :

$$\begin{pmatrix} Z + Z_0 & Z_0 \\ Z_0 & Z + Z_0 \end{pmatrix} \cdot \begin{pmatrix} I_G \\ I_D \end{pmatrix} = \begin{pmatrix} V_G \\ V_D \end{pmatrix}. \quad (\text{C14})$$

On the other hand, the finite frequency admittance of the quantum Hall bar can be obtained from the edge magnetoplasmon scattering matrix which, in the present case is symmetric. We can then infer expressions for the impedances $Z(\omega)$ and $Z_0(\omega)$ in terms of the EMP scattering matrix of the quantum Hall bar:

$$Z_0(\omega) = R_H \frac{S_{\text{d}}(\omega)}{(1 - S_{\text{od}}(\omega))^2 - S_{\text{d}}(\omega)^2}, \quad (\text{C15a})$$

$$Z(\omega) = \frac{R_H}{1 + S_{\text{d}}(\omega) - S_{\text{od}}(\omega)}. \quad (\text{C15b})$$

Note that Eqs. (C15a) and (C15b) have been obtained without any explicit assumption of total screening. In the case of $\eta = 1$ (total screening, see Eq. (C3)), Z_0 is expected to be infinite and is indeed found to be infinite since, in this case, $S_{\text{d}}(\omega) + S_{\text{od}}(\omega) = 1$ (see Eq. (C12b)).

To obtain the simplest effective circuit description, we just derive the dominant terms of the low frequency expansion of $Z(\omega)$ and $1/Z_0(\omega)$ by expanding the edge-magnetoplasmon scattering matrix in powers of ω . This leads to $1/Z_0(\omega) = 0$ (total screening) and

$$Z(\omega) = \frac{R_H}{2} \left(1 - \frac{i\omega l/v_{\text{d}}}{2 + \nu\alpha_{\nu}} \right) \quad (\text{C16})$$

which shows that the impedance $Z(\omega)$ can be viewed as the series addition of a resistance $R_H/2 = R_K/2\nu$ (ν

parallel single channel contact resistances $R_K/2$) and an inductance $L_Z(\nu)$ such that

$$\frac{2L_Z(\nu)}{R_H(\nu)} = \frac{l/2 v_{\text{d}}(\nu)}{1 + \nu\alpha_{\nu}/2}. \quad (\text{C17})$$

The quantum Hall bar is then a dipole with impedance $2Z(\omega)$ which then behaves as an inductance in series with the quantum Hall resistance R_H at low frequency. Since $2L_Z$ is the total inductance L of the quantum Hall bar, it follows that the electronic time of flight l/v_{d} appearing in Eq. (A4) is renormalized by Coulomb interactions. The corresponding renormalized velocity

$$v_{\text{eff}}(\nu) = v_{\text{d}}(\nu) \left(1 + \frac{\nu\alpha_{\nu}}{2} \right) \quad (\text{C18})$$

can, in a sense, be interpreted as an effective charge velocity.

To understand this more precisely, let us imagine that the quantum Hall bar could be viewed as an ideal coaxial cable with ν channels with plasmonic velocity v_P . This would lead to a diagonal plasmon scattering matrix: $S_{\text{od}}(\omega) = 0$ and $S_{\text{d}}(\omega) = e^{i\omega l/v_P}$. The corresponding admittance $Z(\omega)$ would then be given by

$$Z_{\text{tl}}(\omega) = \frac{R_H}{2} \frac{1}{1 + e^{i\omega l/v_P}} \quad (\text{C19})$$

where the index tl emphasizes the transmission line description considered here. Its low frequency expansion would correspond to the series addition of the contact resistance $R_H/2$ with an inductance $L_Z^{(\text{tl})}$ given by

$$\frac{2L_Z^{(\text{tl})}}{R_H} = \frac{l}{2v_P}. \quad (\text{C20})$$

Consequently, we also recover the analogue of Eq. (A4) with v_P playing the role of v_{d} . However, in this transmission line model, the admittance $1/Z_0$ would not vanish, thereby showing that such a transmission line model cannot describe the totally screened situation. The edge magnetoplasmon scattering matrix derived in Sec. C2 shows that, in the totally screened case, R_H/Z_0 vanishes.

Appendix D: Geometric capacitance

In this section, we compute the geometric capacitance of the quantum Hall bar using as model a capacitor built from two coplanar strips corresponding to the two counter-propagating edge channel systems.

1. Width of edge channels

The model of Ref. [28] by Schklovskii *et al.* describes the structure of quantum Hall edge channels when taking into account the effect of Coulomb interactions. It predicts the width λ_H (also denoted by a_{ν} following Ref.

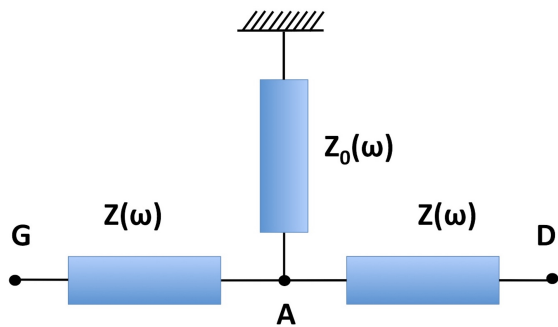


FIG. 9. The lumped element circuit equivalent to simple quantum Hall bar depicted on Fig. 8. The 0 lead corresponds to metallic gates and conductors to which the edge channels are capacitively coupled in the case of partial mutual capacitive coupling between the R and L channels ($\eta < 1$). We expect $\text{Re}(Z(\omega)) = R_H/2$ and $\text{Im}(Z(\omega))$ to be inductive at low frequency whereas $\text{Re}(Z_0(\omega)) = 0$ and $Z_0(\omega)$ is expected to be capacitive in general, and to be infinite in the totally screened case ($\eta = 1$).

[28]) of the incompressible channels in term of the density gradient at the edge as well as the width b_ν of compressible channels as a function of λ_H .

The width of incompressible stripes is obtained by identifying the Landau gap with the energy variation of an electron in the confining potential U_ν (see Figure 10):

$$a_\nu \times e\nabla U_\nu = \hbar \frac{eB}{m^*}, \quad (\text{D1})$$

where ∇U_ν denotes the gradient of U_ν within the incompressible part of the edge of the sample. As explained in the main text, the confining potential may depend on ν as discussed in Sec. D.2. For simplicity, we shall assume that this gradient has indeed the same dependence on ν as the charge transport velocity $v_d(\nu)$ present in the equations of motion (C5) and (C6). This leads to:

$$a_\nu = \frac{\hbar}{m^* v_d(\nu)}, \quad (\text{D2})$$

where we have replaced the drift velocity within the incompressible stripe $(E_y/B_z)_\nu$ by the drift velocity along the edge by $v_d(\nu)$. Note that this expression is formally the Compton wavelength associated with a relativistic particle of mass m^* and effective speed of light $v_d(\nu)$. This explains why we denote it by λ_H in the following. This result is not surprising, the width of the incompressible stripe is the minimal one for closing the cyclotron gap for an electronic excitation in the confinement potential, as shown in Ref. [28].

Once the width of an incompressible stripe is known, the width of a compressible stripe is given by

$$b_\nu = \frac{\pi \lambda_H^2}{4 a_B} \quad (\text{D3})$$

where $a_B = \hbar^2 \epsilon / m^* e^2$ denotes the effective Bohr radius in the material.

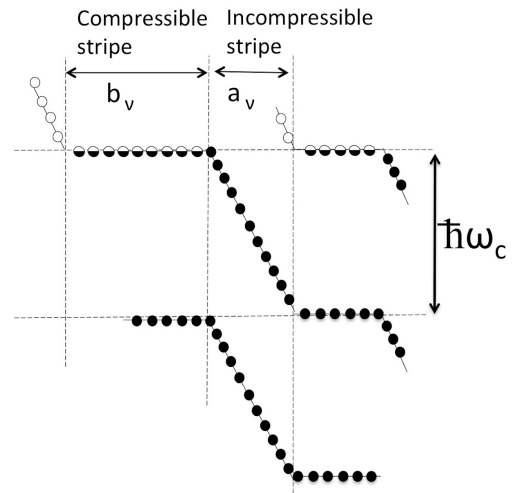


FIG. 10. Edge channel structure arising from Coulomb interaction effects in a mean field theory approach [28]: incompressible stripes alternate with compressible stripes in which electrons are located right at the Fermi energy.

2. On the ν -dependence of $v_d(\nu)$

In this section, we discuss the ν -dependence of the confining potential $v_d(\nu)$. In the regime where no compressible stripes are present, this would be the chiral drift velocity associated with the confining potential at the edge of the sample $v_d = \nabla U / eB$. In the case of a smooth confining potential, compressible stripes may appear and the velocity $v_d(\nu)$ refers to the effective charge velocity at the edge, arising from the dynamics of the compressible stripe coupled to the incompressible one [30]. As explained before, our main hypothesis here is that this velocity can be used in the expressions (D2) and (D3) of the width of incompressible and compressible parts of the edge channels and that it has the same expression for all of them.

We discuss here two different forms for $v_d(\nu)$, one based on Ref. [44] and the other one based on Ref. [45]:

$$v_d(\nu) = \begin{cases} v_d/\nu & \text{following Ref. [44]} \\ v_d/\sqrt{\nu} & \text{following Ref. [45]} \end{cases} \quad (\text{D4})$$

Our discussion will be based on heuristic arguments which only identify $v_d(\nu)$ with a drift velocity if the edge channel does not contain any compressible stripe [62, 63]. However, Han and Thouless have shown in Ref. [30] that, in the presence of the compressible stripe, the velocities of the eigenmodes propagating along the edge channel contain a contribution from the incompressible part drift velocity. We think that this justifies the heuristic arguments that will now be laid down.

In Ref. [44], Mikhailov gave the following form for the

edge velocity of plasmons due to the quantum confining potential: $v_N = \omega_c/k_F$ (Eq. 1-60). As the cyclotron frequency ω_c is inversely proportional to the filling factor ν , and $k_F = \sqrt{2\pi N_s}$ only depends on the density of the 2DEG, this velocity is $v_d(\nu) = v_d/\nu$ with $v_d \sim 4 \times 10^5 \text{ ms}^{-1}$ for our sample.

We have used such velocity in Eq.(1) to fit the data. However, we have varied the numerical parameter around this value to fit our data in Fig. 4. As can be shown from Fig. 4 of the paper, the fitting values of v_d are between 1/4 and 10 times the above estimation.

In Ref. [45], which studies the breakdown of the IQHE, Chaubet and Geniet computed a confining potential by solving the problem of an harmonic oscillator with a boundary condition on the edge. They showed that, when the wave function equals zero at the edge, the eigen-energies are modified compared to the boundary-less problem and increase, giving a realist interpretation of the confining potential. In Fig. 9 of Ref. [45], the confining potential – represented by the energy of states – increases nearly linearly with the distance from the edge. We thus approximate the gradient ∇U_ν by the ratio of the cyclotron energy to the magnetic length: $\nabla U_\nu = \hbar\omega_c/l_B$. The physical image is that the potential slope corresponds to an energy gain of the order of the Landau gap on a length scale l_B . This gives a drift velocity $v_d(\nu) = \sqrt{\hbar e B(\nu=1)/m^* \nu^{-1/2}}$ which in the case of our sample leads to $v_d(\nu) = v_d/\sqrt{\nu}$ with $v_d \sim 3 \times 10^5 \text{ ms}^{-1}$.

Exactly as for the previous model, we have considered v_d as a fit parameter that can be varied in order to represent all experimental situations in our experiments. As can be shown from Fig. 4 of the paper, the fitting values of v_d are between 1/5 and 5 times the above estimation, a smaller range than with the $v_d(\nu) = v_d/\nu$ model.

3. Capacitance computation

The quantum Hall edge channel system has a width

$$W_H(\nu) = \frac{\nu\hbar}{m^*v_d(\nu)} (1 + \pi^2\alpha_{\text{eff}}(\nu)), \quad (\text{D5})$$

which is of the order of 90 nm per edge channel in AlGaAs/GaAs systems. In the transverse direction, the electrons are confined within a triangular potential well. The typical extension of the electron's wavefunction in the transverse direction is of the order of 5 nm [64], therefore suggesting a rather flat shape of the edge channel.

A first estimate of the geometric capacitance of the edge channel system can thus be obtained by computing the geometric capacitance per unit of length of an infinite pair of coplanar strips of width w separated by a distance d [65]:

$$\frac{C_H(l)}{l} = \varepsilon_0\varepsilon_r \frac{K(\sqrt{1-x^2})}{K(x)}, \quad (\text{D6})$$

in which $K(x)$ denotes the elliptic integral of the first kind [66] evaluated at $x = d/(d+2w)$ where, in our case $w = W_H(\nu)$ and $d+2w = W$ is the total width of the quantum Hall bar. Using known asymptotics for the elliptic integral, we find the geometrical capacitance for the quantum Hall bar of width W and length l at filling fraction ν

$$C_H(\nu, l) \simeq \frac{\pi\varepsilon_0\varepsilon_r l}{\ln\left[\frac{W}{8W_H(\nu)}\right]}. \quad (\text{D7})$$

On the other hand, using a more precise self-consistent solution of the electrical potential within quantum Hall edge channel arising from the repartition of quantum electrons, Hirai and Komiyama [67] have shown that the capacitance can be obtained as the geometric capacitance of two parallel wires:

$$c'_0(\nu, l) = \frac{\pi\varepsilon_0\varepsilon_r l}{\ln\left(\frac{eW}{2W_H(\nu)}\right)}. \quad (\text{D8})$$

Expressions (D7) and (D8) are not identical, but both are considered in the regime where $W \gg W_H(\nu)$, that is, when they lead to similar estimates for the capacitance. Both expressions are of the form

$$C_H(\nu, l, \gamma) = \frac{\pi\varepsilon_0\varepsilon_r l}{\ln\left(\frac{\gamma W}{W_H(\nu)}\right)}, \quad (\text{D9})$$

where γ is a factor that depends on the specific model used to describe the charge repartition within the edge channels. Here $\gamma = e/2$ in Harai *et al.*'s estimate and $\gamma = 1/8$ for the coplanar strip capacitance model. Using Eq. (D9), the effective coupling constant is then

$$\alpha_\nu = \frac{2\alpha_{\text{eff}}(\nu)}{\pi} \left[\ln\left(\frac{\gamma W/\lambda_H(\nu)}{(1 + \pi^2\alpha_{\text{eff}}(\nu))\nu}\right) \right]. \quad (\text{D10})$$

Using this expression into Eq. (C18) leads to

$$\frac{v_{\text{eff}}}{v_d} = 1 + \frac{\nu\alpha_{\text{eff}}(\nu)}{\pi} \ln\left(\frac{\gamma W/\lambda_H(\nu)}{(1 + \pi^2\alpha_{\text{eff}}(\nu))\nu}\right) \quad (\text{D11})$$

for the ratio of v_{eff} to the drift velocity within a chiral edge channel. This expression can then be rewritten in terms of the effective single edge channel width $\xi_H(\nu) = (1 + \pi^2\alpha_{\text{eff}}(\nu))\lambda_H(\nu)/\gamma$:

$$\frac{v_{\text{eff}}}{v_d} = 1 + \frac{\nu\alpha_{\text{eff}}(\nu)}{\pi} \ln\left(\frac{W/\xi_H(\nu)}{\nu}\right) \quad (\text{D12})$$

Appendix E: Supplementary results

In this Section, we show further experimental results obtained on sample A (the sample discussed in the paper) and on three other samples manufactured from three different AlGaAs/GaAs heterojunctions. Their wafer

characteristics (electron density and mobility of the two-dimensional electron gas) are reported in table I. Samples have been processed on these heterojunctions using the same design and dimensions as for sample A. Experimental results obtained on these samples have been obtained using exactly the same protocols and they are completely similar to the results presented in the paper.

We first present complementary results on sample A, then we present results obtained on the other samples, which concern influence of filling factor ν and influence of edge channel length.

Wafer	$N_s(\text{cm}^{-2})$	$\mu(\text{m}^2/\text{Vs})$	B (for $\nu = 2$)	Width (μm)
A	5.1	30	10.5 T	400
B	3.3	50	6.8 T	1600
C	4.5	55	9.2 T	400
D	4.3	42	9 T	800

TABLE I. Sample characteristics: carrier density, mobility, magnetic field at $\nu = 2$ and width of Hall bars.

1. Complementary results on sample A

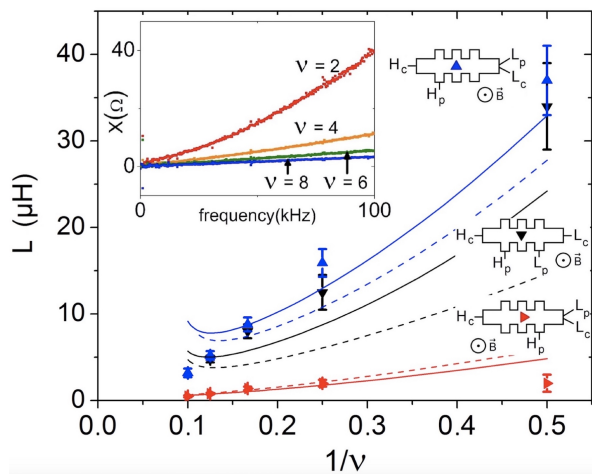


FIG. 11. Kinetic inductance as a function of the inverse of filling factor for a positive orientation of magnetic field. Dashed line represents the model $v_d(\nu) = v_d/\nu$ with following parameters : $v_d = 8 \times 10^5 \text{ ms}^{-1}$ for the $l = 1600 \mu\text{m}$ configuration, $v_d = 11 \times 10^5 \text{ ms}^{-1}$ for the $l = 1000 \mu\text{m}$ one, $v_d = 22 \times 10^5 \text{ ms}^{-1}$ for the $l = 600 \mu\text{m}$ one. In the same way, the continuous lines correspond to the $v_d(\nu) = v_d/\sqrt{\nu}$ model with: $v_d = 1.2 \times 10^5 \text{ ms}^{-1}$ for the $l = 1600 \mu\text{m}$ configuration, $v_d = 0.5 \times 10^5 \text{ ms}^{-1}$ for the $l = 1000 \mu\text{m}$ one, $v_d = 0.5 \times 10^5 \text{ ms}^{-1}$ for the $l = 600 \mu\text{m}$ one. Note that length of edge states are still the same than on Fig. 3 of the paper.

Fig. 3 of the paper shows, for a positive orientation of magnetic field, the dependence of the quantum inertia on the inverse of the filling factor. In Fig. 11, these results have been obtained for a positive orientation of

magnetic field. Once again the models $v_d(\nu) = v_d/\nu$ (dashed lines) and $v_d(\nu) = v_d/\sqrt{\nu}$ have been considered using a proper velocity v_d for each configuration (see caption). Although the agreement between the experimental data and the theory is not as good as in the case of $B < 0$ configurations, we still see that $v_d(\nu) = v_d/\sqrt{\nu}$ better reproduces the data (especially for the $l = 1600 \mu\text{m}$ configuration).

2. Influence of filling factor for other samples

For sample A we have shown that reactance increases linearly with frequency and that the slope depends strongly on the filling factor. Here, we observe the same behavior on other samples (see Figs. 12 to 14): the slope decreases while the filling factor increases.

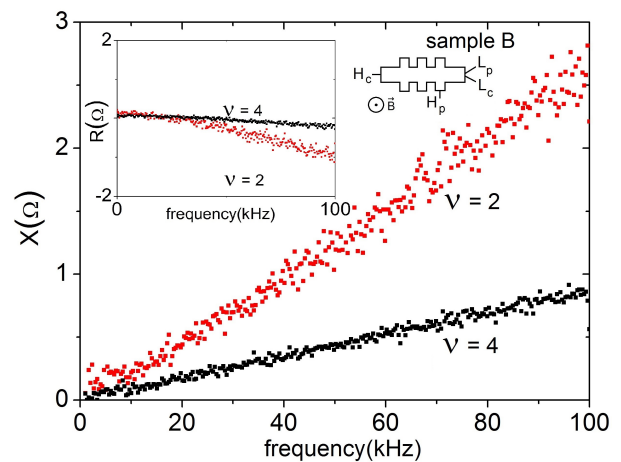


FIG. 12. Reactance as a function of frequency, for sample B and $\nu = 2$ and 4. Configuration is shown in inset.

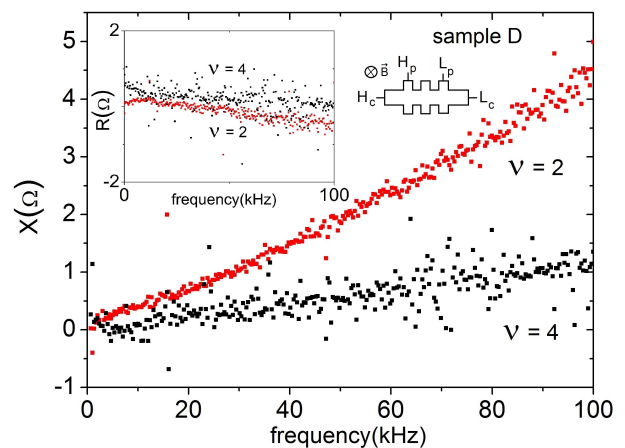


FIG. 13. Reactance as a function of frequency, for sample D and $\nu = 2$ and 4. Configuration is shown in inset.

For Figs. 12, 13 and 14, the data have only been obtained for two values of ν . However, Fig. 15 displays

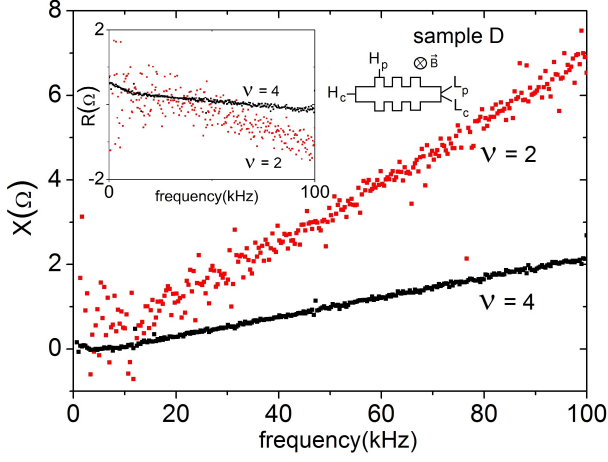


FIG. 14. Reactance as a function of frequency, for sample D at $\nu = 2$ and 4 and configuration shown in inset.

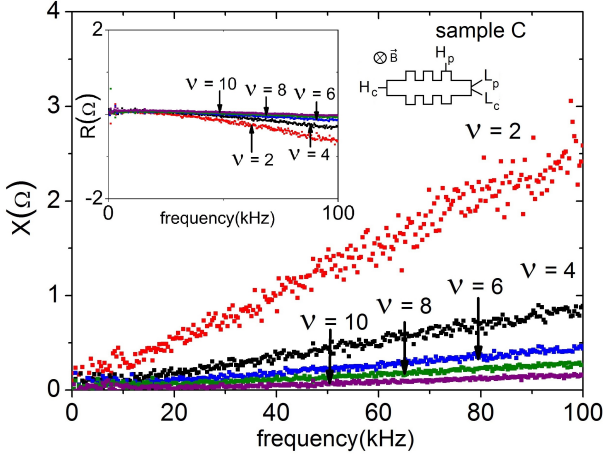


FIG. 15. Reactance as a function of frequency, for sample C and $\nu = 2$ to 10 by steps of 2. Configuration is shown in inset.

all even values of ν from 2 to 10 for sample C in a given configuration. It is then possible to try fitting these experimental data using Eq. (1) of the paper with $v_d(\nu) = v_d/\sqrt{\nu}$. This fit is presented on Fig. 16 and show that our model also described correctly the experimental data for sample C with the configuration displayed on Fig. 15.

3. Influence of configurations for other samples

Figs. 17 to 20 depict the reactance as a function of frequency for three samples at different filling factors. For each sample at a given filling factor, we observe how the

configuration (shown as an inset for each curve) modifies the slope of the reactance. Each configuration has its proper length and the larger the edge states the higher the quantum inertia. The length concerned here is the

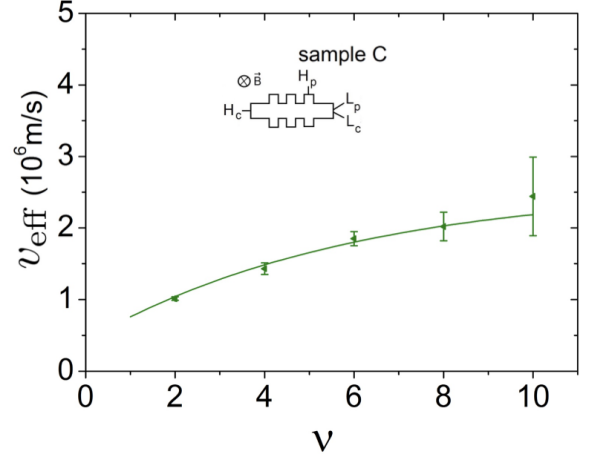


FIG. 16. Plot of the effective velocity $v_{\text{eff}}(\nu)$ obtained from the data displayed on Fig. 15 and fit by Eq. (1) of the paper using $v_d(\nu) = v_d/\sqrt{\nu}$ with $v_d = 2.2 \times 10^5 \text{ ms}^{-1}$.

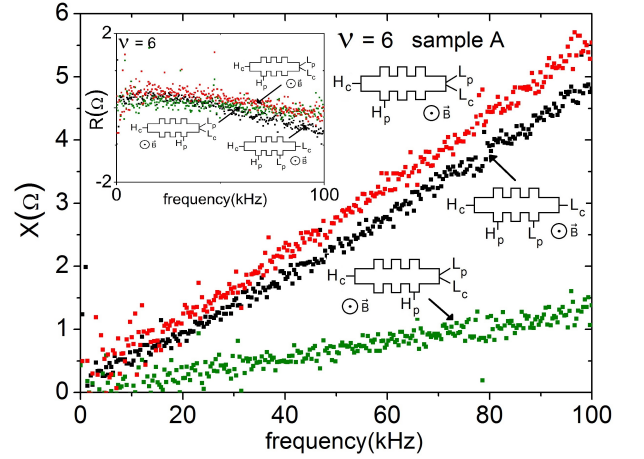


FIG. 17. Reactance as a function of frequency, for sample A at $\nu = 6$ and for the three configurations.

distance between potentials L_p and H_p .

Meanwhile, differences in velocity v_d for distinct configurations imply that the ratio between quantum inertia and length of edge states not a constant. Configurations are obtained after wire-bonding the samples. This entails heating the samples and cool them down again afterwards, and this causes the velocity v_{eff} to change a bit from one configuration to another.

[1] K. v. Klitzing, G. Dorda, and M. Pepper, Phys. Rev. Lett. **45**, 494 (1980).

[2] B. I. Halperin, Phys. Rev. B **25**, 2185 (1982).

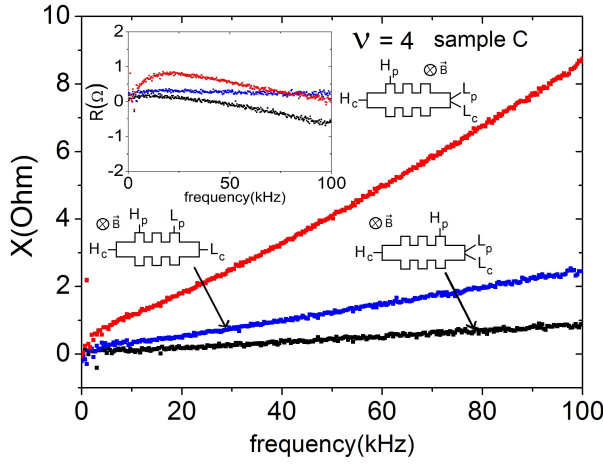


FIG. 18. Reactance as a function of frequency, for sample C at $\nu = 4$ and for the three configurations.

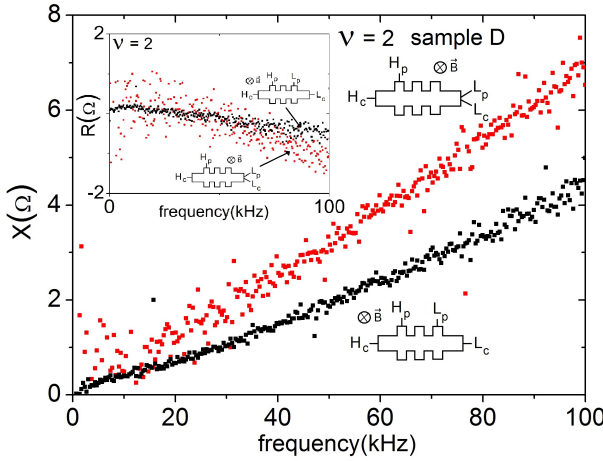


FIG. 19. Reactance as a function of frequency for sample D at $\nu = 2$ for two configurations.

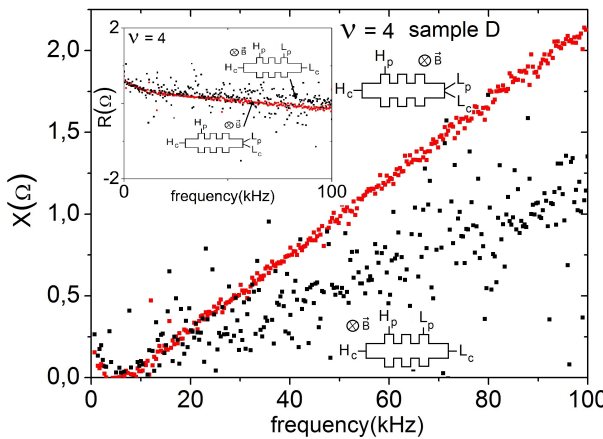


FIG. 20. Reactance as a function of frequency for sample D at $\nu = 4$ for two configurations. Note the smaller values for $X(\Omega)$ compared to the other curves which may explain the more noisy dataset for the four-terminal geometry.

- [3] R. J. Haug, *Semiconductor Science and Technology* **8**, 131 (1993).
- [4] J. Weis and K. von Klitzing, *Philosophical Transactions of the Royal Society A: Mathematical, Physical and Engineering Sciences* **369**, 3954 (2011), <https://royalsocietypublishing.org/doi/pdf/10.1098/rsta.2011.0198>.
- [5] M. E. Suddards, A. Baumgartner, M. Henini, and C. J. Mellor, *New Journal of Physics* **14**, 083015 (2012).
- [6] C. I. des Ponds et Mesures, “Représentation de l’ohm à partir de l’effet hall quantique,” *Recom. 2 (CI-1988)* 77th Session (1988).
- [7] B. Jeckelmann and B. Jeanneret, *Reports on Progress in Physics* **64**, 1603 (2001).
- [8] F. J. Ahlers, B. Jeanneret, F. Overney, J. Schurr, and B. M. Wood, *Metrologia* **46**, R1 (2009).
- [9] F. Delahaye, *Metrologia* **31**, 367 (1995).
- [10] S. W. Chua, A. Hartland, and B. Kibble, *IEEE Transactions on Instrumentation and Measurement* **48**, 309 (1999).
- [11] J. Schurr, B. Wood, and F. Overney, *IEEE Transactions on Instrumentation and Measurement* **54**, 512 (2005).
- [12] M. E. Cage and A. Jeffrey, *J. Res. Natl. Inst. Stand. Technol.* **101**, 733 (1996).
- [13] B. Jeanneret, B. D. Hall, H.-J. Bühlmann, R. Houdré, M. Ilegems, B. Jeckelmann, and U. Feller, *Phys. Rev. B* **51**, 9752 (1995).
- [14] J. Schurr, J. Kučera, K. Pierz, and B. P. Kibble, *Metrologia* **48**, 47 (2011).
- [15] P. J. Burke, *IEEE Transactions on Nanotechnology* **1**, 129 (2002).
- [16] J. Kang, Y. Matsumoto, X. Li, J. Jiang, X. Xie, K. Kawamoto, M. Kenmoku, J. H. Chu, W. Liu, J. Mao, K. Ueno, and K. Banerjee, *Nature Electronics* **1**, 46 (2018).
- [17] A. A. Annunziata, D. F. Santavicca, F. Frunzio, G. Catealani, M. J. Rooks, A. Frydman, and D. E. Prober, *Nanotechnology* **21**, 445202 (2010).
- [18] J. Luomahaara, V. Vesterinen, L. Grönberg, and J. Hassel, *Nature Communications* **5**, 4872 (2014).
- [19] G. Coiffard, K. F. Schuster, E. F. C. Driessen, S. Pignard, M. Calvo, A. Catalano, J. Goupy, and A. Monfardini, *Journal of Low Temperature Physics* **184**, 654 (2016).
- [20] M. Büttiker, A. Prêtre, and H. Thomas, *Phys. Rev. Lett.* **70**, 4114 (1993).
- [21] M. Büttiker, *J. Phys.: Condens. Matter* **5**, 9361 (1993).
- [22] A. Prêtre, H. Thomas, and M. Büttiker, *Phys. Rev. B* **54**, 8130 (1996).
- [23] J. Gabelli, G. Fève, J. Berroir, B. Plaçais, A. Cavanna, B. Etienne, Y. Jin, and D. Glatli, *Science* **313**, 499 (2006).
- [24] J. Gabelli, G. Fève, T. Kontos, J.-M. Berroir, B. Plaçais, D. C. Glatli, B. Etienne, Y. Jin, and M. Büttiker, *Phys. Rev. Lett.* **98**, 166806 (2007).
- [25] L. Song, J. Yin, and S. Chen, *New Journal of Physics* **20**, 053059 (2018).
- [26] M. Büttiker, *Phys. Rev. B* **38**, 9375 (1988).
- [27] S. M. Girvin and K. Yang, *Modern Condensed Matter Physics* (Cambridge university Press, 2019).
- [28] D. B. Chklovskii, B. I. Shklovskii, and L. I. Glazman, *Phys. Rev. B* **46**, 4026 (1992).
- [29] I. L. Aleiner and L. I. Glazman, *Phys. Rev. Lett.* **72**, 2935 (1994).
- [30] J. H. Han and D. J. Thouless, *Phys. Rev. B* **55**, R1926 (1997).

- [31] M. Hashisaka, H. Kamata, N. Kumada, K. Washio, R. Murata, K. Muraki, and T. Fujisawa, *Phys. Rev. B* **88**, 235409 (2013).
- [32] N. Hiyama, M. Hashisaka, and T. Fujisawa, *Applied Physics Letters* **107**, 143101 (2015).
- [33] B. Kibble and G. Rayner, *Coaxial AC bridges* (Taylor & Francis, 1984).
- [34] *Agilent impedance measurement handbook* (Agilent Technologies Inc., 2009).
- [35] M. Grayson and F. Fischer, *Journal of Applied Physics* **98**, 013709 (2005), <https://doi.org/10.1063/1.1948529>.
- [36] C. Hernandez, C. Consejo, P. Degiovanni, and C. Chaubet, *Journal of Applied Physics* **115**, 123710 (2014).
- [37] W. Desrat, D. K. Maude, L. B. Rigal, M. Potemski, J. C. Portal, L. Eaves, M. Henini, Z. R. Wasilewski, A. Toropov, G. Hill, and M. A. Pate, *Phys. Rev. B* **62**, 12990 (2000).
- [38] J. Melcher, J. Schurr, F. Delahaye, and A. Hartland, *Phys. Rev. B* **64**, 127301 (2001).
- [39] Here $R_{xx}(\omega)$ denotes the frequency dependant longitudinal dependence of the quantum Hall bar.
- [40] I. Safi and H. J. Schulz, *Phys. Rev. B* **52**, R17040 (1995).
- [41] I. Safi, *Eur. Phys. J. D* **12**, 451 (1999).
- [42] E. Bocquillon, V. Freulon, J. Berroir, P. Degiovanni, B. Plaçais, A. Cavanna, Y. Jin, and G. Fève, *Nature Communications* **4**, 1839 (2013).
- [43] T. Christen and M. Büttiker, *Phys. Rev. B* **53**, 2064 (1996).
- [44] S. A. Mikhailov, “Edge and inter-edge magnetoplasmons in two-dimensional electron systems,” in *Edge Excitations of Low-Dimensional Charged Systems*, Horizons in World Physics, Vol. 236, edited by O. Kirichuk (Nova Science Publishers, Inc., NY, 2000) Chap. 7, pp. 171 – 198.
- [45] C. Chaubet and F. Geniet, *Phys. Rev. B* **58**, 13015 (1998).
- [46] Additional results obtained on samples from different wafers are presented in Sec. V of the Supplemental Material provide additional evidence of the robustness of our analysis.
- [47] P. Roulleau, F. Portier, P. Roche, A. Cavanna, G. Faini, U. Gennser, and D. Mailly, *Phys. Rev. Lett.* **100**, 126802 (2008).
- [48] N. Kumada, H. Kamata, and T. Fujisawa, *Phys. Rev. B* **84**, 045314 (2011).
- [49] M. Hashisaka, K. Washio, H. Kamata, K. Muraki, and T. Fujisawa, *Phys. Rev. B* **85**, 155424 (2012).
- [50] M. Hashisaka and T. Fujisawa, *Reviews in Physics* **3**, 32 (2018).
- [51] P. Armagnat, A. Lacerda-Santos, B. Rossignol, C. Groth, and X. Waintal, *SciPost Phys.* **7**, 31 (2019).
- [52] P. Armagnat and X. Waintal, *Journal of Physics: Materials* **3**, 02LT01 (2020).
- [53] G. Roussely, E. Arrighi, G. Georgiou, S. Takada, M. Schalk, M. Urdampilleta, A. Ludwig, A. D. Wieck, P. Armagnat, T. Kloss, X. Waintal, T. Meunier, and C. Bäuerle, *Nature Communications* **9**, 2811 (2018).
- [54] E. Bocquillon, V. Freulon, F. Parmentier, J. Berroir, B. Plaçais, C. Wahl, J. Rech, T. Jonckheere, T. Martin, C. Grenier, D. Ferraro, P. Degiovanni, and G. Fève, *Ann. Phys. (Berlin)* **526**, 1 (2014).
- [55] A. L. Grimsmo, F. Qassemi, B. Reulet, and A. Blais, *Phys. Rev. Lett.* **116**, 043602 (2016).
- [56] E. B. Rosa, *Bulletin of the Bureau of Standards* **4**, 301 (1908).
- [57] A. Delgard, B. Chenaud, D. Mailly, U. Gennser, K. Ikushima, and C. Chaubet, *Physica Status Solidi B* **256**, 1800548 (2019).
- [58] A. O. Slobodeniuk, I. P. Levkivskyi, and E. V. Sukhorukov, *Phys. Rev. B* **88**, 165307 (2013).
- [59] P. Degiovanni, C. Grenier, G. Fève, C. Altimiras, H. le Sueur, and F. Pierre, *Phys. Rev. B* **81**, 121302(R) (2010).
- [60] C. Cabart, B. Roussel, G. Fève, and P. Degiovanni, *Phys. Rev. B* **98**, 155302 (2018).
- [61] The l dependence of C_H is restored here to stress that we are in the limit of a long quantum Hall bar ($l \gg W$) where it is linear in l .
- [62] O. G. Balev and P. Vasilopoulos, *Phys. Rev. Lett.* **81**, 1481 (1998).
- [63] I. O. Baleva, N. Studart, and O. G. Balev, *Phys. Rev. B* **65**, 073305 (2002).
- [64] F. F. Fang and W. E. Howard, *Phys. Rev. Lett.* , 797 (1966).
- [65] Y. Y. Iossel, E. Kochanov, and M. G. Strunskiy, *The calculation of electrical capacitance*, Tech. Rep. (Leningradskoye Otdeleniye ”Energiya”., 1969).
- [66] I. Gradshteyn and I. Ryzhik, *Table of integrals, series and products (fifth ed.)* (Academic Press, Inc, 1994).
- [67] H. Hirai and S. Komiyama, *Phys. Rev. B* **49**, 14012 (1994).